JOURNAL OF GEOPHYSICAL RESEARCH, VOL. 95, NO. D6, PAGES 7661–7675, MAY 20, 1990

Cloud Cover Analysis With Arctic Advanced Very High Resolution Radiometer Data
2. Classification With Spectral and Textural Measures

J. KEY

Cooperative Institute for Research in Environmental Sciences, University of Colorado, Boulder

The variation in cloud amount over polar ice sheets, sea ice, and ocean surfaces can have important effects on planetary albedo gradients and on surface energy exchanges, so that monitoring of polar cloud cover is crucial to studies of climate change. The spectral and textural characteristics of polar clouds and surfaces for a 7-day summer series of advanced very high resolution radiometer (AVHRR) data in two Arctic locations are examined, and the results used in the development of a cloud classification procedure for polar satellite data. Since spatial coherence and texture sensitivity tests indicate that a joint spectral-textural analysis based on the same cell size is inappropriate, cloud detection with AVHRR data and surface identification with passive microwave data are first done on the pixel level as detailed in part 1 (Key and Barry, 1989). Next, cloud patterns within (250 km)^2 regions are described, then the spectral and local textural characteristics of cloud patterns in the image are determined and each cloud pixel is classified by statistical methods. Results indicate that both spectral and textural features can be utilized in the classification of cloudy pixels, although spectral features are most useful for the discrimination between cloud classes. This methodology provides a basis for future "objective" automated mapping of cloud types and amount over snow and ice covered surfaces.

1. INTRODUCTION

High-latitude response to changes in cloud cover is a key area of uncertainty in evaluating changes in the global climate system. To better understand climatic forcing, statistical frameworks for describing the morphology of cloud fields as well as the radiative, dynamical, and microphysical processes determining this morphology are needed [*Committee on Global Change*, 1988, p. 117]. Major uncertainties exist in current cloud climatologies for polar regions as a result of the problem of discriminating clouds over snow and ice using satellite visible or infrared data.

This issue has been addressed in part 1 of this research [*Key and Barry, 1989*], where an algorithm was presented that performs pixel-scale analysis of surface and cloud radiances utilizing visible, thermal, and passive microwave data over a 7-day period. The purpose of this paper is to examine the spectral and textural characteristics of summertime polar clouds and surfaces in advanced very high resolution radiometer (AVHRR) data; the issue of the appropriate scale of measurement for texture measures will be addressed, and an optimal set of features is determined. This information is then used in the development of a procedure that classifies cloudy pixels (identified as such by the algorithm described in part 1) into recognizable cloud patterns. The methodology employed differs from other studies in that only the cloudy pixels are classified, in contrast to the method of gridding an image and classifying the grid cells, which themselves may contain mixtures of surface and cloud types. As detailed in a later section, some of the problems that have been recognized with traditional spectral-textural classifiers have been alleviated, but others have been created.

Cloud detection methods for use with satellite data that examine only spectral characteristics of pixels include single-channel and multichannel threshold methods, radiative transfer models, histogram techniques, and statistical clustering procedures. These are reviewed in part 1 [*Key and Barry*, 1989]. Some studies have included an analysis of texture in cloud classification schemes, generally in a clustering framework [e.g., *Welch et al.*, 1988, 1989; *Garand*, 1988; *Ebert*, 1987, 1988, 1989; *Parikh*, 1977]. Contextual analyses of frontal patterns and cloud shadows are given by *Gurney and Townshend* [1983], *Wang et al.* [1983], *Swain et al.* [1981], and the spatial classifier of *Kettig and Landgrebe* [1976].

Global cloud climatologies are reviewed by *Hughes* [1984]. *Vowinckel* [1962], *Huschke* [1969], and *Gorshkov* [1983] provide perhaps the most comprehensive cloud climatologies for the Arctic, but these are derived primarily from surface observations. They show general agreement in the seasonal cycle of total cloud amount but differ in the geographical distribution of cloud cover, particularly in the case of low cloud in winter. Spring and summer cloud amounts and patterns in the Arctic have been recently examined by *Kukla* [1984], *Robinson et al.* [1986], *Barry et al.* [1987], and *McGuffie et al.* [1988]. *McGuffie et al.* [1988] compared three cloud analysis methods (two manual and one automated) based on Defense Meteorological Satellite Program (DMSP) images. While cloud detection schemes exist for many data types and geographic locations, the inherently subjective nature of defining cloud types and the algorithmic difficulty of incorporating texture into the analyses are two inhibiting factors in the development of the automated cloud typing methods needed for large-scale cloud climatologies.

Paper number 89JD03422.
0148-0227/90/89JD-03422$05.00

2. DATA SET

All five AVHRR channels (1, 0.58–0.68 µm; 2, 0.73–1.0 µm; 3, 3.55–3.93 µm; 4, 10.3–11.3 µm; 5, 11.5–12.5 µm) are initially employed. Data from the Nimbus 7 Scanning Multichannel Microwave Radiometer in channels (SMMR) 18 and 37-GHz vertical polarization, as well as SMMR-derived sea ice concentration, are used for surface parameterization in the cloud detection step described in part 1 [*Key and Barry*, 1989] but are not used directly in the analysis of cloud patterns. SMMR, SMMR-derived sea ice concentration, and AVHRR data were coregistered to a polar stereographic projection and used simultaneously. The effective pixel size of the AVHRR data is reduced to 5 x 5 km [*Maslanik et al.*, 1989].

Two areas of the Arctic are examined (Figure 1). One area is centered on the Kara Sea and Barents Sea extending north to the pole and south to Norway and the Siberian coast. The second area covers most of the Canadian archipelago and Greenland, also extending to the pole. A 7-day summer series (July 1–7, 1984) of these two areas is used in the analysis of cloud patterns. These areas include representative samples of all surface types found in the Arctic: snow-covered and snow-free land, sea ice of varying concentrations, open water, and permanent ice cap. The observed conditions are usual for summer in the Arctic, as are the pressure patterns which occurred. Synoptic pressure patterns observed in Arctic Ocean buoy data [*Colony and Munoz*, 1986] during the study period are similar to the mean pattern for the month [*Serreze and Barry*, 1988; *Gorshkov*, 1983]. Although correlations have been observed between synoptic pressure systems, cloud amount, and cloud type [*Barry et al.*, 1987], detailed cloud climatologies for the Arctic are not available and it is therefore more difficult to make such a statement concerning cloud cover.

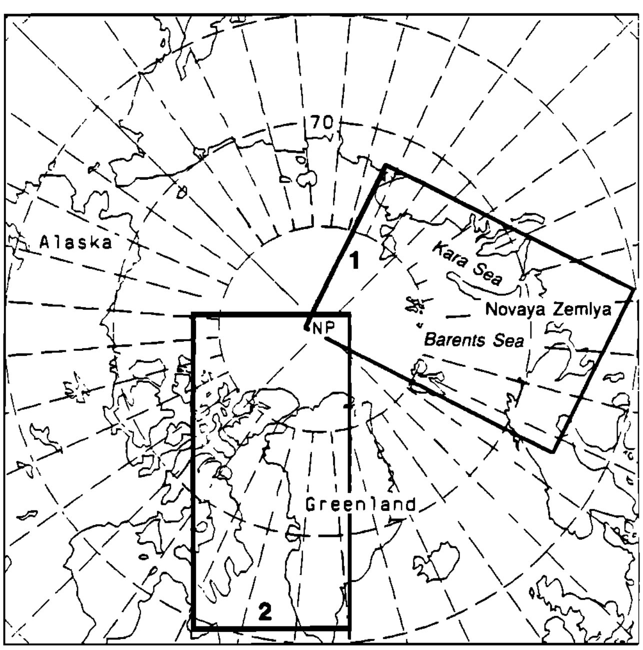

Fig. 1. The two study areas within the Arctic, one centered on the Kara and Barents seas and the other covering much of the Canadian archipelago and northern Greenland.

Area 1 on July 1 exhibits the greatest mixture of cloud patterns and clear-sky conditions of all the imagery and will be used to illustrate the methodology and classification results throughout the remainder of the paper. However, spectral and textural characteristics as well as cloud pattern training areas were extracted from the complete set of imagery, and results are expected to be similar for other days. Figure 2 shows the study area in AVHRR channel 1 (visible). Novaya Zemlya is at upper center with sea ice above and to the left. Sea ice also occupies the lower left portion of the image. Grid lines delineate 50x50 pixel or (250 km)^2 regions. Figure 3 is an image of the cloud-only portion of Figure 2, shown in AVHRR channel 1 (visible) with grid lines delineating cells of 16 x 16 pixels (section 3.3). This image was classified using the algorithm described in part 1 [*Key and Barry*, 1989] and is briefly described in section 4 below. Low thin cloud over sea ice in the Kara Sea, which is not apparent in Figure 2, is identified with AVHRR channel 3 and the temporal tests of the algorithm. Figure 4 is an image of SMMR-derived surface types showing land, sea ice, ice cap, open water, and a narrow coastal zone. Inaccuracies in the identification of cloudy pixels result from incorrect surface identification due to weather effects in the passive microwave, resolution differences between the SMMR and the AVHRR, and coastal effects.

3. FEATURES

3.1. *Spectral Features*

Five surface and three broad cloud classes are analyzed for their spectral characteristics. Surface types are snow-free land, snow-covered land, open water, medium- to high-concentration sea ice, and low-concentration sea ice. Cloud classes are defined by channel 4 brightness temperature (T) assumed to represent temperatures at the top of optically thick cloud layers, and encompass the following categories: low, $T > 265$ K; middle, $245 \leq T \leq 265$ K; and high, $T < 245$ K. Spectral and textural features were calculated only for "pure" classes, i.e., groups of contiguous pixels, or cells, that contain one and only one class as determined through a manual interpretation. Training areas were defined manually.

Spectral features examined for each pixel are channel 1, 2, and 3 reflectance; channel 3, 4, and 5 brightness temperatures; ratios of channels 2 and 1, 3 (reflectance) and 1; and channel 4 minus 5 (brightness temperature difference). The ratio of channel 2 to channel 1 in AVHRR data or the difference between channels 2 and 1 enhances vegetation signals, arctic haze, and snow and sea ice underneath clouds. Channel 3 is important for the discrimination of low clouds over snow and ice surfaces. The difference between channels 3 and 4 aids in the detection of optically thin cloud and fog, while the difference between channels 4 and 5 is useful for identifying cirrus [*Olesen and Grassl*, 1985; *Saunders*, 1986]. For each cell, the mean and standard deviation are examined. These are first-order statistics that describe the distribution of pixel values within a cell.

3.2. *Textural Features*

Second-order statistics summarize the probability of the intensity values of a pair of pixels. These relative frequencies are computed for each pair of pixels in a given

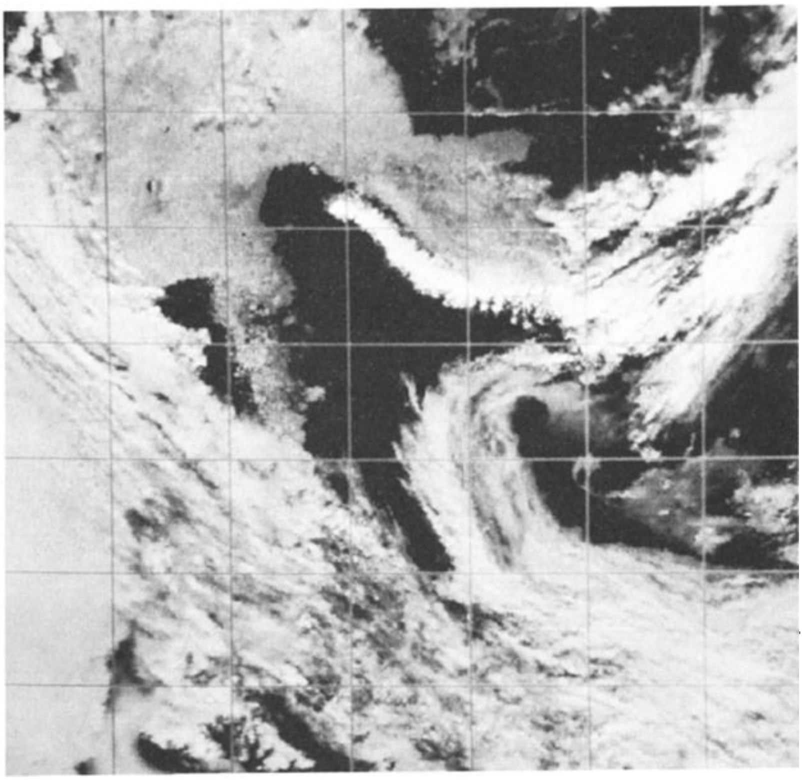

Fig.2. Visible (AVHRR channel 1) image of a portion of study area 1 on July 1, 1984. Novaya Zemlya is at upper center. Grid lines delineate (250 km)^2 regions.

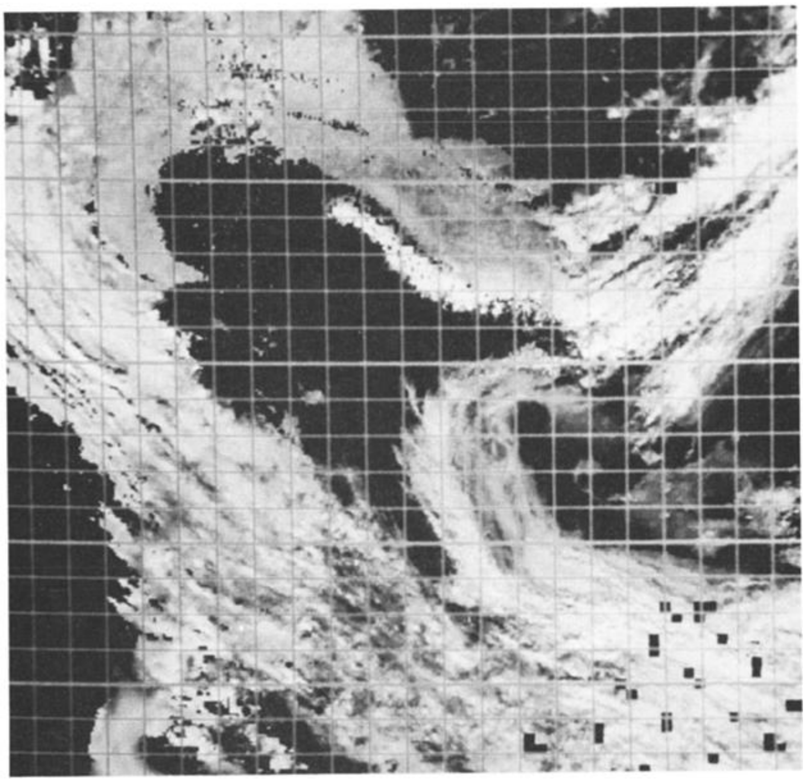

Fig.3. The cloud only portion of Figure 2, as determined following the methodology given in part 1 [*Key and Barry*, 1989]. AVHRR channel 1 (visible) data are shown. Grid lines delineate 16x16 pixel cells, the size used in subsequent texture analyses.

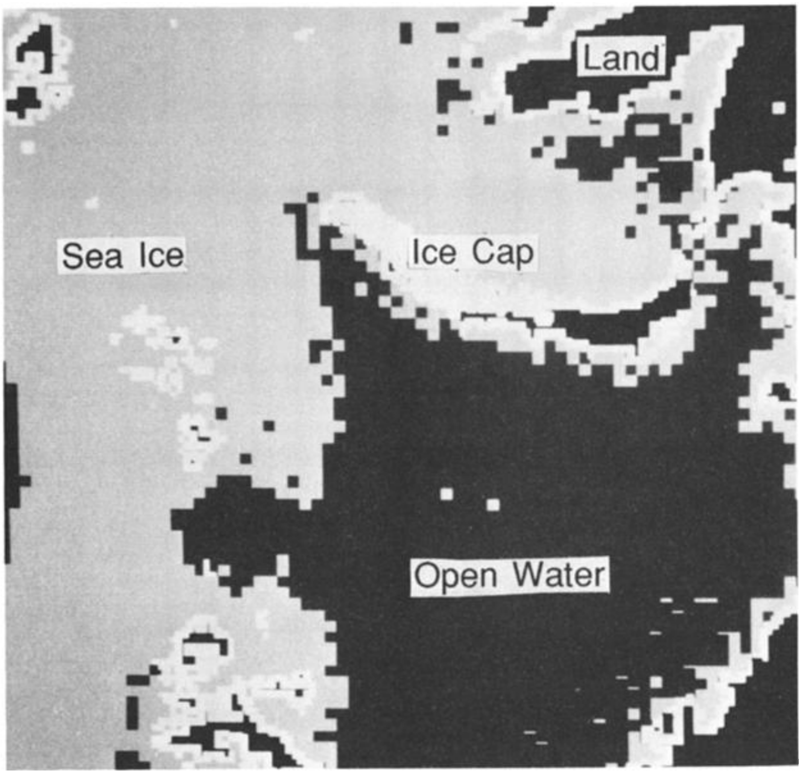

Fig.4. Surface types corresponding to the area shown in Figure 2, from SMMR and SMMR-derived data. Surface categories are land, snow/ice cap, sea ice (all concentrations), open water, and a narrow coastal zone.

positional relationship and are summarized in a grey level cooccurrence matrix (GLCM). Positional relationships refer to separation distance d and direction θ. *Haralick et al.* [1973] first used cooccurrence matrices to classify terrains in aerial photographs with a very small matrix. *Welch et al.* [1988] and *Kuo et al.* [1988] computed a number of measures from the GLCM for cloud analysis. Higher-order textural statistics may also be calculated, although they generally involve more computation and do not necessarily yield better results. *Julesz* [1975] has argued that two textures with identical second-order statistics are not discriminable. It is possible therefore that first- and second-order statistics are all that are needed to discriminate texture.

Weszka et al. [1976] modified this method to operate on grey level difference (GLD) histograms rather than grey level pairs. The data are first quantized to 64 grey levels, and the grey level difference g is computed for each pair of pixels in the cell over each of four angles: up-down (0°), left-right (90°), upper left–lower right (135°), upper right–lower left (45°). Texture may contain a directional component so that the histogram must be specified as a function of angle as well as distance. A histogram of gray level differences is then constructed for each distance and angle and used to compute various texture measures. The histograms will be spread over a larger range of g as graininess or streakiness increases. The grey level difference texture measures calculated from the histograms are the mean, contrast, angular second moment, and entropy for the cell. The mean, maximum, and range of these quantities over the four angles are used in subsequent analyses. Both GLD and GLCM texture measures were initially computed for the AVHRR data sets. However, because of the similarity of these measures, only the GLD measures were retained because they are computationally simpler.

The variability of grey level differences is summarized by the contrast. Large values correspond to structured clouds such as cumulus with shadows. The angular second moment measures the homogeneity of gray level differences with distance and direction. Angular second moment will be high for decks of stratus and for bands of clouds oriented in the direction of θ. Entropy describes the degree to which distinct scales of organization are unrecognizable. It is maximum when all radiance differences have an equal probability of occurring (i.e., the histogram is uniform) and low when texture is smooth. See the appendix for more detail and definitions of the texture measures.

If texture is coarse and d is small compared with the texture element size, the pairs of points at separation d will usually have similar gray *levels* and the histogram will have high frequencies around g=0. Conversely, with fine texture and d comparable to element size, the gray level differences will often be large with a large spread in the frequencies of g. If texture is directional and d is in the proper range, the degree of spread in the histogram should vary with direction. Separation distances of 1, 2, 4, and 8 have been examined elsewhere [e.g., *Weszka et al.*, 1976; *Parikh*, 1977], with distances of 1 or 2 preferred. *Welch et al.* [1988] found that optimal separation distance depends on cloud type. However, the effect of pixel resolution on textural features is unclear. Since a small cell size is used here (discussed below), and because separation distances of 1 and 2 function similarly in this data set, d=1 is used.

Other texture measures are also examined. The area-averaged Roberts gradient is maximum in regions of sharp brightness contrast and is therefore a measure of edge strength [e.g., *Gonzalez and Wintz*, 1977]. It is defined over any separation distance but does not have directional sensitivity. *Hobson* [1972] and *Harris and Barrett* [1978] utilize a measure called vector strength. If the pixels within a cell are connected into a set of adjacent triangular planes, then texture can be measured through the dispersion in three-dimensional space of normal vectors to these planes. Vector strength is a summary of the distribution of normal vectors and is high for smooth surfaces and low for rough surfaces.

A two-dimensional Fourier transform [e.g., *Bunting and Fournier*, 1980] is also applied to each cell as a means of defining the texture of cyclical cloud patterns. Three measures are used: the streakiness factor, cell intensity, and the maximum ring density wavelength. The streakiness factor is a directional measure which takes on values between 0 and 1, values near 1 being highly directional [*Garand*, 1988]. Cell intensity is the proportion of power in the spectrum associated with wavelengths between 20 and 40 km, the typical size of convective cells [*Agee and Dowell*, 1976]. The maximum ring density wavelength is the wavelength of the center of the annular ring in the power spectrum with the maximum density, where the spectrum is divided into four rings. The spectral and textural features are summarized in Table 1, where abbreviations used in the remainder of the text are also given.

These texture measures are calculated for the five surface classes defined previously, and for 12 cloud classes which include some of the basic cloud groups and mixtures of these as observed in the data: (1) Low thin cloud over water (stratus); (2) Low thin cloud over ice (stratus); (3) Low thin cloud over land (stratus); (4) Low thick cloud, smooth texture (stratus); (5) Low thick cloud, bumps or broken (stratocumulus); (6) Middle cloud rolls (broken, linear altostratus usually over a stratiform layer); (7) Broken middle cloud, not linear; (8) Middle thick cloud, smooth (altostratus, possibly over stratus); (9) Middle/high bumps (cirrocumulus or altocumulus); (10) High thick cloud with some middle cloud (broken cirrostratus over altostratus); (11) High thick cloud, smooth (cirrus or cirrostratus); (12) Cumulus. The surface was included in classes 1–3 only because the clouds are thin and differed primarily in albedo. Contributions from surfaces to cloud albedo or temperature in the other classes was not significant enough to justify defining additional classes. Class 7 is similar to class 6 but occurred at a higher altitude (lower temperature).

3.3. *Cell Size*

The issue of cell size is important in that too large a cell may blur the boundaries between classes, while too small a cell may not permit adequate description of the textural and spectral features which distinguish between the classes. In addition, the larger the number of pixels in each cell, the more reliable the statistical estimates will be. A number of cell sizes have been used in previous

TABLE 1. Summary of AVHRR Spectral and Textural Measures

Feature	Abbreviation
Single Pixel Spectral Measures	
Channel 1, 2, 3 reflectance	CH01, CH02, CH03
Channel 3, 4, 5 brightness temperature	CHT3, CHT4, CHT5
Ratios: 2/1, 3/1	RA21, RA31
Brightness temperature difference: channels 4 and 5	DF45
Cell Spectral-Textural Measures (Channels 1,3,4)	
Spectral mean	MEAN
Standard deviation	SD
Grey level difference (mean, maximum, range over four directions)	
Mean	MMEAN, XMEAN, RMEAN
Contrast	MCON, XCON, RCON
Angular second moment	MASM, XASM, RASM
Entropy	MENT, XENT, RENT
Roberts gradient	RG
Vector strength	VECTOR
Fourier measures	
Streakiness factor	SF
Cell intensity	CI
Maximum ring wavelength	WAVE

cloud classifications; for example, *Ebert* [1987] clustered 32 x 32 (128 km)^2 AVHRR cells; *Garand* [1988] analyzed 64 x 64 (128 km)^2 GOES cells; *Wu et al.* [1985] examined 20 x 20 and 5 x 3 (20 km)^2 GOES -2, SMS -2, and GOES -4 cells in a study of rainfall; *Weszka et al.* [1976] used 64 x 64 Landsat -1 cells; *Parikh* [1977] computed texture from 64 x 64 (205x355 km) NOAA -1 data; *Haralick and Shanmugam* [1974] introduced many of the texture measures described with 64 x 64 (7.5 square miles) ERTS - 1 data; and *Welch et al.* [1988] used 512 x 512 (29 km)^2 Landsat cells. Cell sizes seem to be chosen somewhat arbitrarily, although cell size has been chosen as a power of 2 in those studies which employ the fast Fourier transform. The cell size used here was based on a number of measures, both quantitative and qualitative.

In an attempt to quantify the effect of cell size, the texture measures were calculated for the cloud and surface classes using cell sizes of 4 to 24 in increments of 2 with a separation distance of 1. Generally the texture values either remain essentially unchanged or decrease/increase linearly for cells of size 24 down to 16. Cell sizes of 10 or less often produce highly variable texture values. Values for cells of size 12 and 14 are similar to those with sizes 16 and larger but are more variable. A paired t test for the difference between cell sizes, with the null hypothesis that there is no difference between the means, indicates that there appears to be a difference between cells of sizes 8, 16, and larger (0.05 level of significance). In no cases can we conclude that there is a significant difference between texture measures extracted from cells of sizes 14 and 16, 16 and 18, and 14 and 18. Other pairs show results between these two extremes. These results are reasonable if we wish to maximize the number of texture elements within a cell. Usually, these basic texture elements exist on a smaller scale; for example open convective cells are 20–40 km and cloud rolls which have wavelengths of approximately 40 km. Additionally, *Garand and Weinman* [1986] found that cloud texture is best measured over mesoscale regions, of the order of 100–250 km square. The approximate lower limit in the above analyses is 16 x 16 pixels, or (80 km)^2 at the 5-km pixel mapping.

In addition to capturing the basic texture of a class, we are also interested in ensuring that as many cells as possible in an image represent only one class. The pixels within a cell containing a relatively uniform surface should exhibit a high degree of spatial coherence and therefore have a relatively low standard deviation when compared to a cell which contains a boundary between two classes that are widely separated in feature space. To further investigate the effects of different cell sizes, a single-channel synthetic image was created which consists of rectangular "objects" of varying sizes and locations. The minimum and maximum allowable sizes of objects are specified. An object is generated whose dimensions are randomly chosen within the restricted range, and the class of the object is randomly assigned (uniform random number generator). Regions are filled with data for that class with a Gaussian random number generator based on a specified mean and standard deviation. A grid of size 300 x 300 "pixels" was generated with subregions of sizes 5 to 40 pixels, representing objects of sizes 25–200 km. Each of these areas was then assigned a class number from 1 to 6. Means of cells of sizes 2, 6, 10, 14, 18, and 22 pixels square were then calculated, and their relative frequency distributions were examined. These are shown in Figure 5 for cell sizes of 6 to 22. Classes in the synthetic data set with means of 10, 30, 50, 70, 90, and 110 (the standard deviation of each class is 1.5) are well represented by means of 6 x 6 cells and poorly represented by 22 x 22 cells. Cells with means between the class means contain one or more boundaries. In all cases but the last, each of the class means is apparent in the histogram, with mixing increasing with increasing cell size.

Cells representing single classes will exhibit a mean very near the class mean and will have a small standard deviation. In determining which cell size is optimal, these cells are located in the histograms, and the change in their relative frequency with changing cell size is observed. We accept as "pure" cells which have standard deviations no greater than a small percentage of the range of the data, as defined by the spatial coherence method of *Coakley and Bretherton* [1982]. The relative frequency histogram of these cells is then determined (Figure 5, horizontal bars). The figure shows differences between the frequency of pure cells with means the same as the class means and the frequency of all cells with those means. This difference tends to increase with increasing cell size and is attributable to cells which contain a mixture of classes and therefore have large standard deviations. This indicates that classifications which rely solely on cell means for discriminating between classes are likely to have a high error rate. Next, peaks in the histogram of pure cells are examined to determine the probability that the grouping would occur by chance; i.e., that the peak and surrounding intervals represents a uniform distribution. These probabilities are given by a multinomial distribution function. This test of separability shows that two classes are lost with cells of size 14, three are lost when cells of size 18 are used, and none are represented by cells of size 22.

Based on these tests, a cell size of 10 pixels square is the approximate upper limit of spatial coherence if an image is uniformly gridded. Conversely, a cell size of 16 seems to be the approximate lower limit for texture analysis. This discrepancy implies that a joint spectral-textural analysis based on the same cell size is inappropriate. For the following texture analyses of pure classes, a cell size of 16 is used. Of course, these tests apply to this data set only. See *Welch et al.* [1989] for a discussion of resolution effects on texture measures.

3.4. *Choice of Features*

There will undoubtedly be a high degree of redundancy in the spectral and textural variables available for analysis. Benefits in terms of processing as well as interpretability are gained by reducing this set of features to a set that includes only those containing the greatest amount of discriminatory information for the classes of interest. To create this set for cloud-surface analysis using the AVHRR imagery, correlations between features over all classes were examined through principal component analysis (PCA), both unrotated and rotated (Varimax). It is also possible to examine correlations between pairs of variables in a correlation matrix, as has been done by *Garand* [1988] and *Ebert* [1987]. Since variables which have large loadings on the same component generally have large

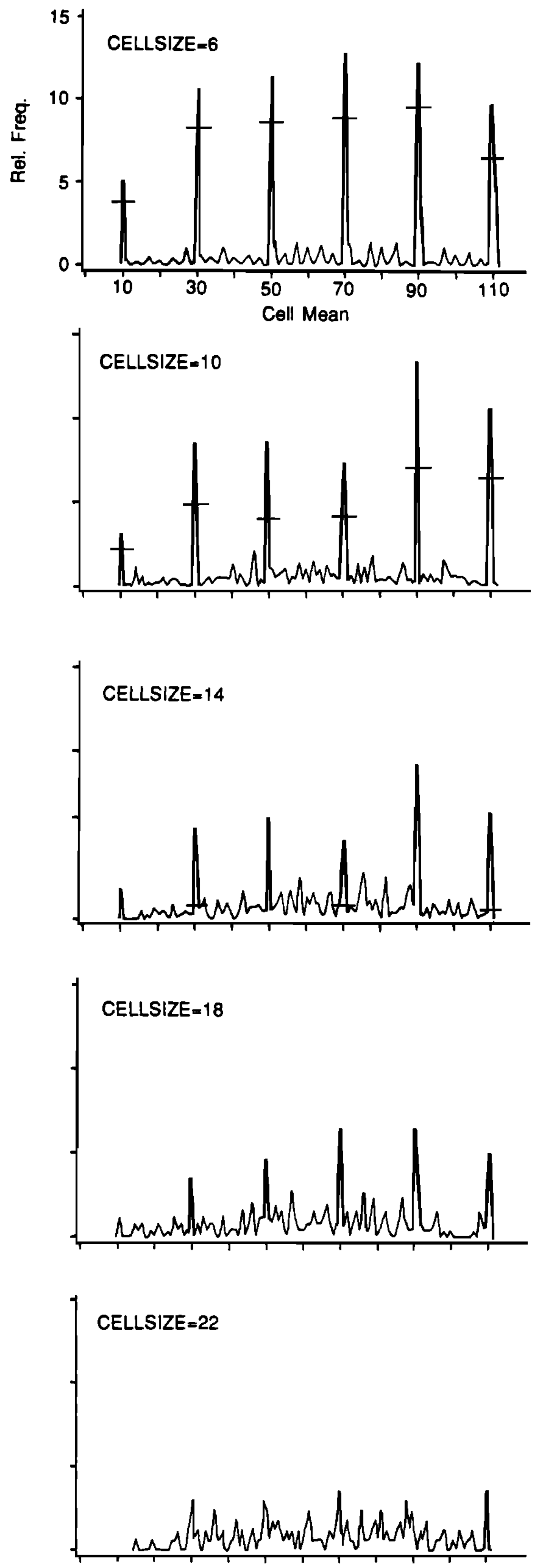

Fig.5. Effect of cell size on the computation of the mean of all cells over an artificially generated data set. Means of classes are 10, 30, 50, 70, 90, and 110. The plots show the relative frequency of cells with various means, indicating mixtures of classes. Horizontal bars show frequency of "pure" cells, i.e., cells containing only one class.

correlations between themselves, this method provides little additional information.

Principal component analysis was applied to both study areas, and the original nine spectral features were reduced to four components with eigenvalues greater than 1.0. Components with eigenvalues less than 1.0 account for less variance than the original variable and are not retained. It is also recognized that beyond the first few components, patterns may be essentially random. The representation of each component is listed in Table 2. The first component represents channel 3, the 3-4 difference, and the ratio of channel 3 to channel 1. Component II represents channels 4 and 5; channels 1 and 2 load highly on component III; component IV represents only the 4-5 difference. The 2/1 ratio loaded highly on component V, but its eigenvalue was only 0.5.

The discriminatory capability of features for all pairs of classes was also determined using a divergence parameter, Fisher distance, defined as

$$D_{ijk} = \frac{|\mu_{ij} - \mu_{ik}|}{\sigma_{ij} + \sigma_{ik}}$$

where μ_i is the mean for variable i on class j or k and σ_i is the corresponding standard deviation. The divergence parameter measures the ability of the feature to differentiate between classes and is computed for each variable and each pair of classes. The higher divergence values correspond to greater usefulness in distinguishing between classes, where $D_{ijk} > 1.0$ has discriminatory skill and $D_{ijk} < 0.5$ generally has poor separating power [*Garand*, 1988]. The number of times a variable ranked first, second, etc., in Fisher distance was tabulated in matrix form. Since PCA implies that of the nine original features only three or four are statistically independent, the top four ranked features for each class pair are most important. Channel 1 scores highest most often followed by channel 2 and channel 4. The ratio features 2/1 and 3/1 and channel 3 follow in rank.

The number of features can now be reduced even further on the basis of the joint results of PCA and divergence calculations. Since channel 1 scored higher more often than channel 2 and since they are highly correlated, channel 2 was eliminated and channel 1 retained. Similarly, channel 4 was retained and channel 5 eliminated. The channel 3 features were similar in discriminatory capability so any could be retained. These two features are of particular interest in discriminating between water and ice clouds. The 4-5 difference did poorly in divergence ranking and would be of little value in this classification application.

The same PCA and divergence parameter methods were applied to the spectral and textural features calculated for the 16 x 16 pixel cells. PCA identified 12 components with eigenvalues greater than 1.0. Table 3 lists these components and which variables they represent. The first three components represent most of the variables and provide an obvious division of the three channels. This indicates that texture measures within a channel vary together to a stronger degree than between channels. This result is important when considering the utility of spectral and textural variables in classification studies.

The results of the divergence parameter testing for the texture measures are given in Table 4. RG, VECTOR,

TABLE 2. The First Four Principal Components of the Nine Spectral Variables.

Component	Features	Variance, %
1	Channel $\underline{3}$, 3-4 difference, 3/1 ratio	27.0
2	Channels $\underline{4}$ and 5	25.5
3	Channels $\underline{1}$ and 2	25.1
4	4-5 difference	12.0
	TOTAL	89.6

Underlined features are used in the final classification.

TABLE 3. First Twelve Principal Components of the Textural Variables.

Component	Features	Variance, %
1	Channel 4: all except those listed below	23.2
2	Channel 3: all except those listed below	19.4
3	Channel 1: all except those listed below	18.2
4	Channel 1: MEAN, VECTOR MASM, XASM	7.0
5	Channel 3: RASM, RENT	
	Channel 4: RASM	4.9
6	Channel 1: RASM, RENT	3.9
7	$MEAN_3$	2.4
8	CI_1, $RCON_{1,3,4}$*	2.2
9	SF_3, $WAVE_3$*	2.1
10	CI_3	1.8
11	SF_4, $WAVE_1$, CI_1*	1.8
12	CI_4, $WAVE_4$, $WAVE_3$*	1.7
TOTAL		88.6

Subscripts refer to AVHRR channel numbers.

*Loading ≤ 0.4; no large loading on any component.

TABLE 4. Texture Variables Retained After Divergence Parameter Analysis

Channel	Texture Features
1	$\underline{RG^3}$, $\underline{VECTOR^4}$, $MMEAN^3$, $XMEAN^3$, $MASM^4$, $\underline{XASM^4}$, $\underline{MENT^3}$, $RENT^6$, $\underline{XENT^3}$, $\underline{SD^3}$
3	RG^2, $VECTOR^2$, $MMEAN^2$, $XMEAN^2$, $MASM^2$, $XASM^2$, $MENT^2$, $XENT^2$, SD^2
4	$\underline{RG^1}$, $\underline{VECTOR^1}$, $\underline{XASM^1}$, $\underline{MENT^1}$, $\underline{SD^1}$

Underlined features ranked highly for cloud class pairs and are used in the final analysis.
Superscripts refer to principal components.

XASM, MENT, and SD ranked high in all three channels. XASM, XENT, and XMEAN indicate that directionality is an important component to the texture of some of the classes. With most pairs of classes, the spectral MEAN and SD features ranked higher than the GLD texture measures.

The angular second moment, vector strength, and entropy texture measures are most useful in surface-cloud discrimination. Specifically, snow-water-land and cloud texture differences were best described by angular second moment and entropy while ice and cloud differences appeared in the vector strength and entropy measures. Entropy was also important in discriminating between the cloud classes. Differences between ice concentrations appeared in the Roberts gradient, entropy, and vector strength. Overall, spectral features were most important for discriminating between surface types, this being in agreement with the findings of *Ebert* [1987]. Entropy and angular second moment were also chosen in the cloud texture analyses of *Welch et al.* [1988] and *Ebert* [1987, 1988].

When the divergence parameter ranking is considered for pairs of cloud classes only, the number of useful texture measures is reduced even further. Channel 3 texture measures did not rank as highly as channel 1 and 4 measures. In the latter two channels, the Roberts Gradient, vector strength, maximum angular second moment, mean entropy, and standard deviation ranked highly most often and are used in the final analysis of cloud patterns.

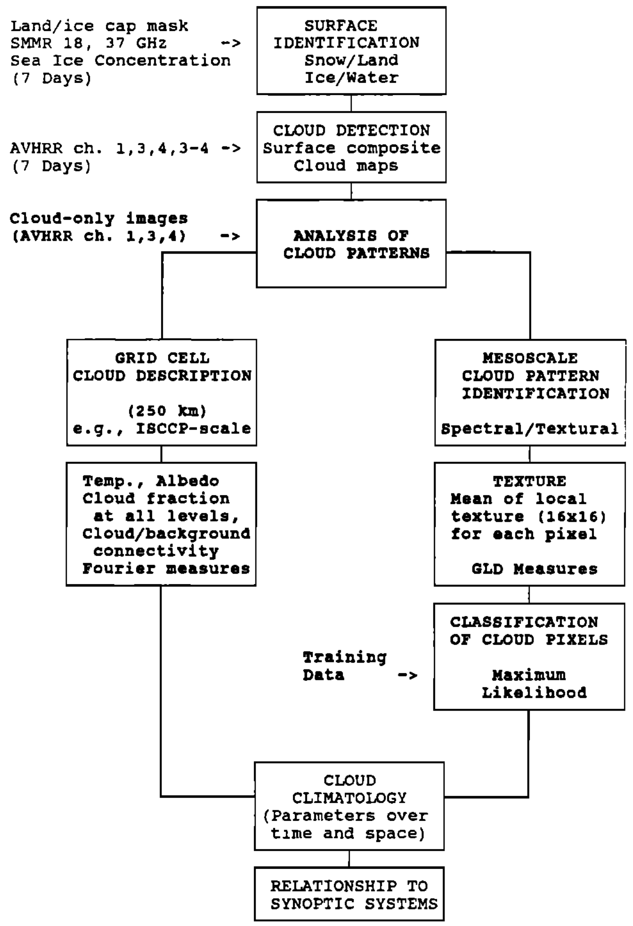

Fig.6. Flow chart of the cloud analysis procedure. Cloud detection is addressed in part 1 [*Key and Barry*, 1989]. The analysis of cloud patterns is done both for (250 km)^2 regions, and over the entire image utilizing spectral and local textural measures. In the latter case, pixels are classified with a maximum likelihood procedure.

4. CLOUD PATTERNS

The cloud analysis methodology employed here includes cloud detection on the pixel scale, a description of cloud patterns on a regional scale, and a classification of cloudy pixels based on spectral and local textural characteristics. This procedure is summarized in Figure 6. The cloud detection procedure is described in part 1 [*Key and Barry*, 1989], and is based on the major steps of an International Satellite Cloud Climatology Project (ISCCP) test algorithm [*Rossow et al.*, 1985]. In the current procedure, surface identification with SMMR and SMMR-derived data sets is the first step. The algorithm then proceeds through a series of steps, each of which is designed to detect some of the clouds present in the scene. Temporal variability at each pixel location is examined for an initial detection of cloudy conditions, and clear-sky composite maps for a 5-day period are produced. A multispectral threshold test of the original data with the clear-sky composites yields a final cloud/no-cloud labeling of the original data.

The two methods of cloud pattern analysis are presented for different purposes: in one case (left side of Figure 6), simple measures are used to describe the characteristics of clouds which occur in regions with artificially defined boundaries. The size of the regions is consistent with that used by the ISCCP and some climate models. The second method is presented as an attempt to eliminate the problems inherent in analyses that impose artificial boundaries on cloud and surface patterns, that being the mixture of different classes within a single cell. It differs from other analyses that have incorporated texture analyses in that only the cloudy pixels are examined; surface pixels are identified in the cloud detection step. Additionally, texture values are assigned to each pixel rather than to a grid cell, and classification of pixels is performed. Other studies have utilized texture to identify both surface and cloud classes and have employed statistical classifiers to distinguish between the two [e.g., *Garand*, 1988; *Welch et al.*, 1988; *Ebert*, 1987]. In supervised classification procedures, training patterns have often included mixtures of cloud and surface types.

The bottom two boxes in Figure 6 identify future work in the automated analysis of cloud patterns and their relationships with synoptic variables. As a part of this goal, the compilation of statistics for cloud fraction, temperature, and number of clouds per grid box is accomplished by the procedure shown in the left side of the figure. However, the comparison of recognizable cloud morphologies (identified through texture analysis shown in the right side of the figure) to gridded synoptic data is the more complex goal and will be the focus of future research.

4.1. *Description of Cloud Within Regions*

Mesoscale analysis is performed within regions that are $(250\ \text{km})^2$, 50 x 50 pixels, or approximately 2.5° latitude by 2.5° longitude (Figure 2). Cloud properties are computed for the cloud-only portion of each region and include overall cloud fraction, cloud fraction at three levels, and connectivity measures. Low, middle, and high cloud amounts were estimated as the percentage of pixels of temperature, T, such that

Low	T_s-13 < $T \le T_s$
Middle	T_s-39 < $T \le T_s$-13
High	$T \le T_s$-39

where T_s is the surface temperature estimated by the clear-sky composite value in AVHRR channel 4.

Cloud connectivity features [*Garand*, 1988] can be extracted from a binary image where each pixel is classed as either cloudy or clear. Cloud connectivity is smaller for highly disconnected elements such as cumulus and larger for uniform stratus decks. Cloud pixels connected only diagonally belong to a different entity, whereas cloud pixels connected above, below, left, or right belong to the same cloud entity. In this manner, the number of clouds and the number of background areas may be counted. If $h_c(i)$ and $h_b(j)$ are the number of pixels in the cloud entity i and the background entity j, respectively, and if we rank the clouds and background areas from smallest to largest, the cloud connectivity CC is defined as

$$CC = h_c(k) \,/\, (mA_c) \qquad A_c > O$$

where A_c is cloud fraction, m is the number of pixels in the image, and k is the cloud number in the ranked list such that

$$\Sigma\ h_c(i) \ge mA_c \,/\, 2 \qquad i=1,k$$

If A_c = 0, CC = 1. Background connectivity is similarly defined as

$$\text{BC} = h_b(k') \,/\, [m(1-A_c)] \qquad A_c \ne 1$$

where k' satisfies

$$\Sigma\ h_b(j) \ge m(1-A_c)/2 \qquad j = 1,k'$$

If A_c = 1, then BC = 1. Background connectivity is a good detector of holes and is low for open cells such as those associated with convective patterns.

The proportion of thin cloud within a region was estimated from the number of cloud pixels with a large difference between channels 3 and 4. On the basis of on empirical studies with the summer data, and following *Saunders* [1986] and *Olesen and Grassl* [1985], if the difference between these two channels exceeds 3.5 K, then the cloud is considered to be thin. This applies to cloud at any height.

Finally, the three-power spectrum measures, streakiness factor, cell intensity, and maximum ring density wavelength, are useful in describing the structure of clouds. Although in the divergence parameter analysis they were less useful in discriminating between cloud classes than the grey level difference measures, they are nonetheless important descriptors and are easier to interpret. Additionally, the methods of feature selection were based on "pure" classes, not the mixtures that will often occur within the artificial boundaries imposed here.

Two of the parameters described above are shown in Figure 7 for the study area, where regional values of low cloud fraction and cloud connectivity are mapped.

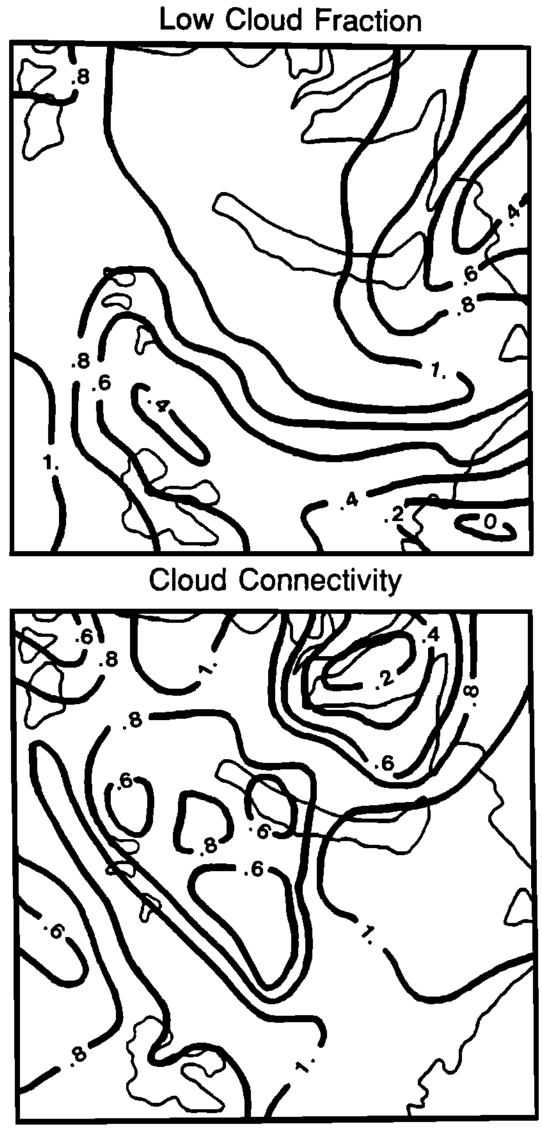

Fig.7. Low cloud fraction and cloud connectivity determined for each $(250\ \text{km})^2$ region within the study area shown in Figure 2. Cloud connectivity (CC) is smaller for highly disconnected cloud elements and larger for connected elements. By definition, CC is set to 1 if overall cloud fraction within a region is 0.

4.2. *Cloud Classification With Spectral and Textural Measures*

The second method of examining cloud patterns is to classify each cloud pixel based on its spectral and local textural characteristics. AVHRR channels 1, 3, and 4 are used as the spectral features. Textural features include those given in Table 4 (underlined) and are determined for each pixel in the following manner. A 16 x 16 pixel cell is moved across the image shifting two pixels at a time. At each location, if the cell contains at least 80% cloud, each texture measure is computed. The value of texture for the cell is assigned to each pixel. With this method, each pixel may be assigned as many as $16^2/2$=128 values. The mean of these values is the value finally assigned to the pixel.

While this method does not eliminate the problem of mixtures of classes within a cell, it does provide a value that is generally representative of the texture within the neighborhood, although when edges between cloud classes are present, the value will be skewed. Figure 8 is an image of the maximum angular second moment GLD measure in AVHRR channel 1 computed over the study area. Large values (lighter grey shades) indicate smooth cloud layers and correspond to both the low and middle level cloud decks seen in Figure 2. Similarly, the darker areas correspond to inhomogeneous grey level pairs, primarily the mixtures of clouds at all levels in cellular or linear patterns.

The maximum likelihood classifier (MLC) [cf., *Ebert* 1987; *Garand*, 1988] is employed; the potential problems and alternatives are discussed in the next section. The 12 cloud classes defined in section 3.2 are used in the classification. A priori probability for each class is 1.0. The classification results are shown in Figure 9 with cloud classes as listed in section 3.2. Only those cloud classes that occurred in the image and were identified by the MLC are shown. Comparison of the results with other classifications is complicated by the subjectivity inherent in defining cloud classes, which are based on those observed in the imagery chosen as a function of both their textural and spectral characteristics. Error analysis implies that there is a correct classification, which at best is difficult to define. For this reason, the discussion is limited to a comparison of Figure 9 with the manual classification shown in Figure 10. Differences are given in Table 5, which is a contingency table showing the percent of pixels classified by each method into each of the classes. Overall classification agreement is 68.3% with 10.3% of the image left unclassified. The largest differences are due to (1) differences in the location of boundaries between cloud systems, (2) labeling of low thin cloud over ice as low thick cloud by the MLC (Kara Sea), (3) the MLC detecting a linear pattern in some middle cloud areas which appeared broken in the manual interpretation, and (4) some low thick cloud areas labeled as middle broken by the MLC. Additionally, the cumulus complex to the left of Novaya Zemlya (Figures 2 and 10) was missed completely by the MLC apparently because of a combination of an insufficient number of training samples and the large number of noncloud pixels within the complex which decreased the number of cells for which texture was computed. Table 5 also shows the percent of each training area correctly classified by the MLC. These values indicate that there is close correspondence between the information classes and the statistical classes except for broken middle cloud (class 7) and, to a lesser degree, middle cloud rolls (class 6). From these observations it can be seen that the classification results could be improved by redefinition of these classes and by choosing more appropriate training areas. However, given the complexity of the problem of how to define and classify cloud patterns the areas in which this method performed poorly are more informative than tuning the classifier to achieve a high classification accuracy.

Comparisons of the MLC results to other methods are also problematic. The question of how this classification would compare to one utilizing only spectral features, for

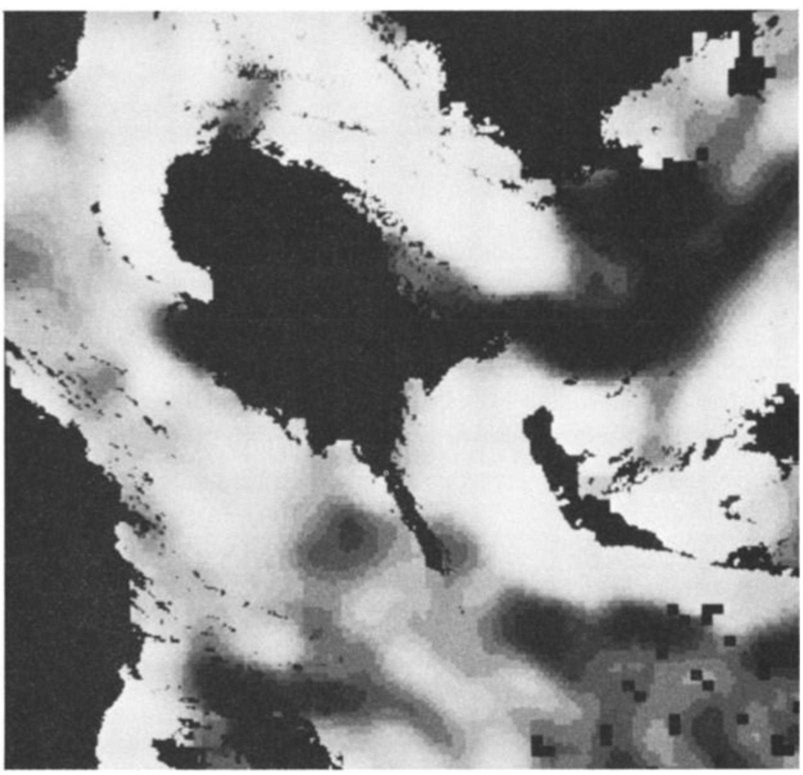

Fig.8. Texture of the clouds within the study area as measured by the maximum angular second moment in AVHRR channel 1. The procedure of moving windows and averaging to obtain texture for each pixel was used. See text for details. Lighter grey shades represent uniform cloud decks.

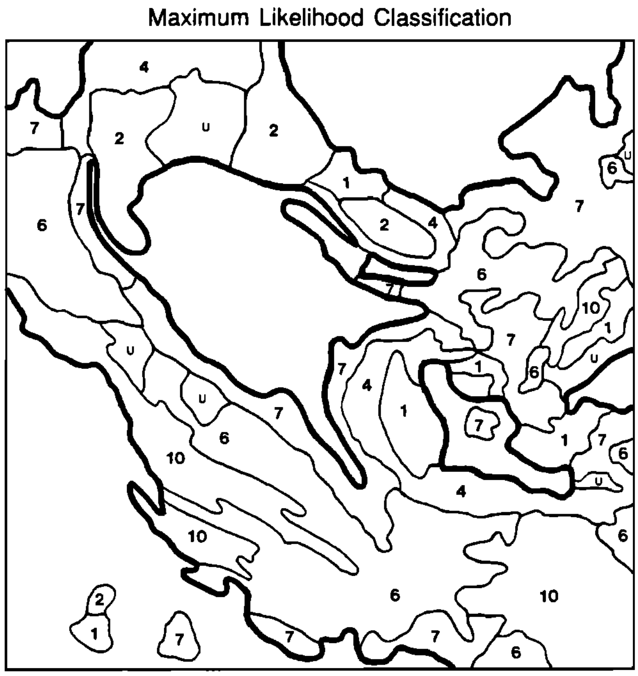

Fig.9. Maximum likelihood classification of cloudy pixels based on their spectral and local textural values. Cloud classes are 1, low thin cloud over water; 2, low thin cloud over ice; 4, low thick cloud smooth; 6, middle cloud rolls; 7, broken middle cloud, not linear; 10, high/middle broken; 12, cumulus. Additionally, clear (bold lines) and unclassified (U) areas are shown.

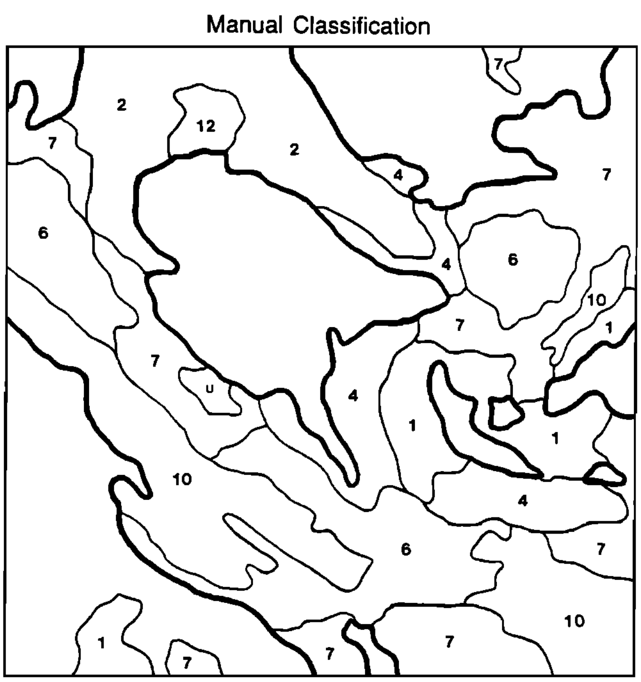

Fig.10. Manual classification of the cloud patterns shown in Figure 3. Classes are the same as in Figure 9.

example, is inappropriate because in such a case the cloud classes would have to be defined without a textural component. In this study we examine the results of the principal components and divergence parameter analyses to obtain some indication of the importance of textural measures in distinguishing between classes. The question of how this classification compares with one that uses texture for fixed grid cells is similarly complicated by the fact that in the fixed grid method, some of the defined classes would include mixtures of cloud types. For example, *Ebert* [1987] employed many of the same texture measures as are used here to classify 32 x 32 pixel grid cells in AVHRR polar images. Some of the 18 classes included mixtures of surface and cloud types. In that study, an MLC classification algorithm was optimized by an iterative procedure incorporating both manual interpretations and statistical assessments of class separability, redefining classes when necessary. The initial model had an accuracy of 55.5% which increased to 84.6% with the optimization. Since the focus of this paper is on an alternative model rather than the optimization of that model, and although similar improvement in accuracy could be expected, such a procedure was not employed.

4.3. *Alternate Methodologies*

Within this procedural framework of cloud pattern analysis starting from a map of cloudy pixels, a number of other methods of textural analysis and classification could be chosen. This is largely an image-processing problem, and as such detailed analyses of the differences of using, for example, one classifier over another are beyond the scope of this paper. Still, it is useful to mention some of the alternatives which may effect the resulting classification.

A maximum likelihood procedure is employed for the segmentation, although arguments could be made for using other procedures, for example, Euclidean distance [*Ince*, 1987] or fuzzy sets [*Key et al.*, 1989] clustering algorithms. Since texture and spectral response are not always equally important in identifying the cloud types, a classifier which allows weighting the different sources of information for each class would be useful. Such a method is proposed by *Benediktsson and Swain* [1989].

Related to the choice of classification method, the question of the normality of distributions of features used in the MLC is an important one and is addressed in detail by *Ince* [1987]. When training areas comprise data from a large geographic area and/or time period, a single informational class (e.g., land albedo) may consist of more than one statistical class. This is certainly the case in the data set employed here, as a chi-square goodness-of-fit test has shown for some of the spectral and textural features extracted over a number of images in different locations and time. However, in a restricted spatial and temporal domain, the normal distribution may provide an adequate model. This is the case in the study area of Figure 2, where chi-square tests show distributions to be approximately normal.

The objective of the moving texture grid cell is to assign the most appropriate texture value to each pixel, one which best represents the texture of the cloud class to which the pixel belongs. Toward this end, other methods of extracting information from the distribution of texture values for a given pixel may be more appropriate than the mean, for example using the median or mode(s). In some cases these would provide more representative values in that boundaries between overlapping cloud layers would

TABLE 5. Percent of the Study Area (Figure 2, Including Surface Areas) Predicted for Each Class by the Maximum Likelihood Classification (Horizontal) Shown in Figure 9 and the Manual Interpretation (Vertical) Shown in Figure 10.

Manual Class	Maximum Likelihood Class (MLC) 1	2	4	6	7	10	% Correct	% TA* Correct
1	2.96	0.27	0.54	0.01	0.57	0.05	75.5	100.0
2	0.83	5.05	1.73	0.06	0.04	0.00	92.7	95.7
4	0.12	0.11	2.70	0.49	1.69	0.01	48.5	99.8
6	0.00	0.00	0.08	10.04	1.40	0.56	58.3	89.4
7	0.01	0.00	0.49	4.82	6.80	0.56	64.2	72.2
10	0.00	0.00	0.03	1.79	0.09	7.67	86.7	95.4
Total (MLC)	3.92	5.45	5.57	17.21	10.60	8.85		

See text for class number references. Cloud occupies 51.6% of the image. Also given is the percent correctly classified in each class. Total percent correctly classified: 68.3.
* Percent of training areas correctly classified by the MLC.

be less blurred, but the computational burden would increase. Ideally, texture would be computed only for homogeneous regions, which of course require texture to be defined. In some cases it may be appropriate to follow a region growing procedure based on temperature, for example, where cloud patterns are grown out of homogeneous pixels which are spatially connected [e.g., *Kettig and Landgrebe*, 1976]. The texture of these regions would then be determined, and if more than one characteristic texture is found, the region could be split.

5. CONCLUSIONS

The cloud analysis methodology presented here provides an alternative to the traditional method of gridding an image, computing spectral and textural features for each cell, and then classifying the cells. Simulations indicate that in such methods, cells small enough to retain a high degree of spatial coherence may be too small to adequately measure texture in the AVHRR GAC data set. Our method includes cloud detection on the pixel scale, a description of cloud patterns on a regional scale, and a classification of cloud pixels based on spectral and local textural characteristics. The cloud detection step involves surface identification, tests of temporal variability at each pixel location, clear-sky compositing over a 5-day period, and a multispectral threshold test of the original data with the clear-sky composites for a final cloud/no-cloud labeling.

From this point, two methods of cloud pattern analysis are presented. In one case, simple measures are used to describe cloud types which occur in $(250\ \mathrm{km})^2$ regions with artificially defined boundaries. Such parameters as cloud fraction at three levels, cloud connectivity, and Fourier measures of cloud cover structure within the regions are computed. These descriptors may be useful for applications which require gridded data, for example, in climate models. The second method is presented as an attempt to eliminate the problems inherent in analyses which impose artificial boundaries on cloud and surface patterns, that being the mixture of different classes within a single cell. Each pixel receives as its texture value the mean value of all cloudy cells to which it belongs. Cloud pixels are then classified by their spectral and textural features following a maximum likelihood procedure.

This methology differs from others which have incorporated cloud texture analyses in two important ways: only the cloudy pixels are examined (surface pixels are identified in the cloud detection step), and texture values are assigned to each pixel rather than to a grid cell. In this manner, training classes can be defined on the basis of texture and do not need to include mixtures of cloud and/or surface classes. However, the subjectivity inherent in defining cloud types makes an objective assessment of the accuracy of the results difficult. This problem is compounded in the test data, where cloud systems are complex. With classes defined in part by texture, comparisons to spectral-only classifications are not appropriate. The test case resulted in 68% of the cloud pixels being correctly classified when compared with a manual interpretation, although no redefinition of classes or training areas was done to increase this value.

Correlation between spectral and textural features and the discriminatory capability of each indicates that spectral features are most useful in discriminating between polar surface and cloud classes but that a few texture measures, such as angular second moment, vector strength, and entropy, as well as standard deviation, retrieve structural information of clouds.

The classification results indicate that as expected, cloud fields are organized into recognizable mesoscale morphologies. An analysis of cloud morphology may in turn give some indication of the physical state of the atmosphere. A detailed examination of the relationship between cloud patterns and synoptic variables requires greater spatial coverage than examined here, as well as a procedure to correlate the cloud patterns (derived with the procedure presented above) to other meteorological data sets. The development of such a procedure is the subject of future research.

APPENDIX

The concept of grey level difference is used to compute the grey level texture statistics [*Weszka et al.*, 1976]. The grey level difference g is computed for each pair of pixels in the cell. A histogram $h_{\theta,d}(g)$ of grey level differences is then constructed for each distance d and angle θ and is used to compute various texture measures. Pixels to the right and left of the pixel being examined are at an angle of 0°, those above and below are at 90°, the upper right and lower left are at 45°, and the upper left and lower right are at 135°. Texture may contain a directional component so that the histogram must be specified as a function of angle as well as distance. Here, spectral values are quantized into 64 equal intervals, based on the expected range in each channel (e.g., for channel 4, the minimum is approximately 220 K, while the normal maximum is 295 K).

The texture measures calculated from the histograms $h_{\theta,d}(g)$ are the mean, contrast, angular second moment, and entropy for the cell. These are defined as

$$MEAN\ (\theta,d) = \frac{1}{64} \sum_g g \frac{h_{\theta,d}(g)}{H_{\theta,d}}$$

$$CON\ (\theta,d) = \sum_g g^2 \frac{h_{\theta,d}(g)}{H_{\theta,d}}$$

$$ASM\ (\theta,d) = \sum_g \left(\frac{h_{\theta,d}(g)}{H_{\theta,d}} \right)^2$$

$$ENT\ (\theta,d) = \sum_g \frac{h_{\theta,d}(g)}{H_{\theta,d}} \ln \frac{h_{\theta,d}(g)}{H_{\theta,d}}$$

$$g = 0,1,\ldots,63$$

where $H_{\theta,d}$ is the total number of grey level differences calculated for distance d and angle θ. The mean, maximum, and range of these quantities over the four angles are used in the classification.

The area averaged Roberts gradient [e.g. *Gonzalez and Wintz*, 1977] is defined as

$$RG = \frac{\sum_{m=1}^{M-d} \sum_{n=1}^{N-d} \left[|B(m,n) - B(m+d,n+d)| + |B(m+d,n) - B(m,n+d)| \right]}{(M-d)(N-d)}$$

where d is the separation distance across which RG is computed.

Vector strength considers the cell of pixels as a set of adjacent triangular planes rather than a set of density points, and texture is then measured through the dispersion in three-dimensional space of normals (vectors) to the cell planes. Triangular planes are constructed by connecting midpoints of a pixel and two of its neighbors. The value of each vertex of the triangle is the value of the corresponding pixel. An number of possibilities for triangle construction exist; here the right and below neighbors are used, as well as the above and left.

Let (l_i,m_i,n_i) be the direction cosines of the ith plane, which are calculated from the coordinates of the normal vector to the plane (x,y,z) by

$$\cos\alpha = x/w$$
$$\cos\beta = y/w$$
$$\cos\delta = z/w$$

where

$$w = (x^2 + y^2 + z^2)^{1/2}$$

The plane normal is calculated as the cross product of two vectors that are known to be on the plane (translated to the origin), the most convenient being the two which form the right triangle of the plane.

The ratio of R to N where N is the number of plane normals and

$$R = [(\Sigma l_i)^2 + (\Sigma m_i)^2 + (\Sigma n_i)^2]^{1/2}$$

is the vector strength and has a value near unity for a smooth surface (e.g., stratus deck) and near zero for an uneven surface (e.g., a cumulus cloud).

Two-dimensional Fourier analysis of spectral data may be used to obtain information on the extended structure of a cloud field, especially where that structure consists of a repeating pattern in either or both dimensions. The Fourier transform of the image $f(k,l)$ is

$$Q(u,v) = 1/KL \sum_{k=0}^{K-1} \sum_{l=0}^{L-1} f(k,l) \exp[-2i\pi(ku/K + iv/L)]$$

$$u = 0,1,\ldots,K-1;\ v = 0,1,\ldots,L-1$$

where K and L are the dimensions of the cell over which the transform is computed. The power spectrum intensity PS(u,v) is defined as the sum of the squared values of the real and imaginary parts of the transform. Three features are used to summarize the power spectrum: the streakiness factor, cell intensity, and the maximum ring density wavelength. The streakiness factor SF, which detects directional patterns [*Garand*, 1988], is

$$SF = \frac{|\sum_u \sum_v uvPS(u,v)|}{[\sum_u \sum_v u^2PS(u,v) \sum_u \sum_v v^2PS(u,v)]^{1/2}}$$

$$u = 0,1,\ldots,K-1;\ v = 0,1,\ldots,K-1;\ (u,v) \neq (0,0)$$

If the pattern has a north-south or east-west orientation, SF=0. To avoid this problem, SF is also evaluated with the axes rotated 45°, and the maximum SF is retained. The cell intensity CI is the proportion of power in the spectrum associated with wavelengths between 20 and 40 km and is defined as

$$CI = \sum_u \sum_v PS(\lambda) \Big/ \sum_u \sum_v PS(u,v)$$

$$u = 1,2,\ldots,K-1;\ v = 1,2,\ldots,K-1;\ 20 \leq \lambda \leq 40$$

$$\lambda = K\rho/(u^2+v^2)^{1/2}$$

where ρ is the spacing between observations (i.e., 5 km in the AVHRR-SMMR data set) and PS(λ) refers to all spectral density estimates with wavelengths λ between 20 and 40 km. More cellular patterns have higher CI values. The maximum ring density wavelength, WAVE, is a scalar representation of the annular area of the spectrum with the maximum density. The density within a ring with radii r_1,r_2, RDW, is given as

$$RDW(r_1,r_2) = \sum_u \sum_v PS(u,v)$$

$$r_1^2 \leq u^2+v^2 \leq r_2^2$$

The power spectrum is divided into four rings, each $K/4$ in u,v dimensions, and the wavelength of the center of the ring with the maximum density is retained.

Acknowledgments. This work was supported under NASA grant NAG-5-898. Thanks are due to W. Rossow and E. Raschke for providing AVHRR GAC data, and to R.G. Barry, J.A. Maslanik, and the reviewers for their comments on an earlier version of this paper.

REFERENCES

Agee, E. M., and K. E. Dowell, Observational studies of mesoscale cellular convection, *J. Clim. Appl. Meteorol.*, *13*, 46-53, 1974.

Barry, R. G., R. G. Crane, A. Schweiger, and J. Newell, Arctic cloudiness in spring from satellite imagery, *J. Climatol.*, *7*, 423-451, 1987.

Benediktsson, J. A., and P. H. Swain, A method of statistical multisource classification with a mechanism to weight the influence of the data sources, *IGARSS'89, 12th Can. Symp. Remote Sens.*, 417-420, 1989.

Bunting, J. T., and R. F. Fournier, Tests of spectral cloud classification using DMSP fine mode satellite data, *Environ. Res. Pap., 704, AFGL-TR-80-0181*, 42 pp., Air Force Geophys. Lab. Hanscom Air Force Base, Mass., 1980.

Committee on Global Change, *Toward an Understanding of Global Change*. National Research Council, National Academy Press, Washington, D.C., 1988.

Coakley, J. A., and F. P. Bretherton, Cloud cover from high-resolution scanner data: Detecting and allowing for partially filled fields of view, *J. Geophys. Res.*, *87*(C7), 4917-4932, 1982.

Colony, R., and E. A. Munoz, Arctic Ocean buoy program, data report, 227 pp., Polar Sci. Cent., Univ. of Wash., 1986.

Ebert, E., A pattern recognition technique for distinguishing surface and cloud types in the polar regions, *J. Clim. Appl. Meteorol.*, *26*, 1412-1427, 1987.

Ebert, E. E., Classification and analysis of surface and clouds at high latitudes from AVHRR multispectral satellite data, *Sci. Rep. 8*, Dep. of Meteorol., Univ. of Wis., Madison, Wis., February 1988.

Ebert, E., Analysis of polar clouds from satellite imagery using pattern recognition and a statistical cloud analysis scheme, *J. Appl. Meteorol.*, *28*, 382-399, 1989.

Garand, L., Automated recognition of oceanic cloud patterns, 1, Methodology and application to cloud climatology, *J. Clim.*, *1*, 20-39, 1988.

Garand, L., and J. A. Weinman, A structural-stochastic model for the analysis and synthesis of cloud images, *J. Clim. Appl. Meteorol.*, *25*, 1052-1068, 1986.

Gonzalez, R. C., and Wintz, P., *Digital Image Processing*, 431 pp., Addison-Wesley, Reading, Mass., 1977.

Gorshkov, S.G. (Editor), *World Ocean Atlas*, vol. 3, Pergamon, New York, 1983.

Gurney, C. M., and J. R. Townshend, The use of contextual information in the classification of remotely sensed data, *Photogramm. Eng. Remote Sens.*, *49*(1), 55-64, 1983.

Haralick, R. M., and K. S. Shanmugan, Combined spectral and spatial processing of Landsat data, *Remote Sens. Environ.*, *3*, 3-13, 1974.

Haralick, R. M., K. Shanmugam, and I. Dinstein, Textual features for image classification, *IEEE Trans. Sys. Man. Cybern.*, *SMC-3*, 610-621, 1973.

Harris, R., and E. C. Barrett, Toward an objective neph- analysis, *J. Appl. Meteorol.*, *17*, 1258-1266, 1978.

Hobson, R. D., Surface roughness in topography: quantitative approach, in *Spatial Analysis in Geomorphology*, edited by R.J. Chorley, Harper and Row, New York, 393 pp., 1972.

Hughes, N. A., Global cloud climatologies: A historical review, *J. Clim. Appl. Meteorol.*, *23*, 724, 1984.

Huschke, R. E., Arctic cloud statistics from "air-calibrated" surface weather observations, *RAND Corp. Mem. RM-6173-PR*, p.79, RAND, Santa Monica, California, 1969.

Ince, F., Maximum likelihood classification, optimal or problematic? A comparison with the nearest neighbour classification, *Int. J. Remote Sens.*, *8*(12), 1829-1838, 1987.

Julesz, B., Experiments in the visual perception of texture, *Sci. Am.*, *232*, 24-43, 1975.

Kettig, R. L., and D. A. Landgrebe, Classification of multispectral image data by extraction and classification of homogeneous objects, *IEEE Trans. Geosci. Elect.*, *GE-14*(1), 19-26, 1976.

Key, J., and R. G. Barry, Cloud analysis with Arctic AVHRR data, 1, Cloud detection, *J. Geophys. Res.*, *94*, 18,521–18,535, 1989.

Key, J. R., J. A. Maslanik, and R. G. Barry, Cloud classification using a fuzzy sets algorithm: a polar example, *Int. J. Remote Sens.*, *10*(12), 1823-1842, 1989.

Kukla, G. J., Variation of Arctic cloud cover during summer 1979, part 1, *Tech. Rep. LDGO-84-2*, Lamont-Doherty Geolog. Observ. of Columbia Univ., Palisades, New York, 1984.

Kuo, K. S., R. M. Welch, and S. K. Sangupta, Structural and textural characteristics of cirrus clouds observed using high spatial resolution LANDSAT imagery, *J. Appl. Meteorol.*, *27*(11), 1242-1260, 1988.

Maslanik, J. A., J.R. Key, and R. G. Barry, Merging AVHRR and SMMR data for remote sensing of ice and cloud in the polar region, *Int. J. Remote Sens.*, *10*(10), 1691-1696, 1989.

McGuffie, K., R. G. Barry, A. Schweiger, D. A. Robinson, and J. Newell, Intercomparison of satellite-derived cloud analyses for the Arctic Ocean in spring and summer, *Int. J. Remote Sens.*, *9*(3), 447-467, 1988.

Olesen, F., and H. Grassl, Cloud detection and classification over oceans at night with NOAA-7, *Int. J. Remote Sens.*, *6*(8), 1435-1444, 1985.

Parikh, J. A., A comparative study of cloud classification techniques, *Remote Sens. Environ.*, *6*, 67-81, 1977.

Robinson, D. A., G. J. Kukla, and M. Serreze, Arctic summer cloudiness, in *Proceedings of the Sixth Conference on Atmospheric Radiation*, p. 176, American Meteorological Society, Boston, Mass., 1986.

Rossow, W. B., F. Mosher, E. Kinsella, A. Arking, M. Desbois, E. Harrison, P. Minnis, E. Ruprecht, G. Seze, C. Simmer, and E. Smith, ISCCP cloud algorithm intercomparison, *J. Clim. Appl. Meteorol.*, *24*, 877-903, 1985.

Saunders, R. W., An automated scheme for the removal of cloud contamination from AVHRR radiances over western Europe, *Int. J. Remote Sens.*, *7*(7), 867-886, 1986.

Serreze, M. S., and R. G. Barry, Synoptic activity in the Arctic Basin, 1979-85, *J. Clim.*, *1*(12), 1276-1295, 1988.

Swain, P. H., S. B. Vardeman, and J. C. Tilton, Contextual classification of multispectral image data, *Pattern Recognition*, *13*, 429-441, 1981.

Vowinckel, E., Cloud amount and type over the Arctic, *Meteorol. Publ.*, *51*, p. 27, Arctic Meteorol. Res. Group, McGill Univ., Montreal, Canada, 1962.

Wang, S., D. B. Elliot, J. B. Campbell, R. W. Erich, and R. M. Haralick, Spatial reasoning in remotely sensed data, *IEEE Trans. Geosci. Remote Sens.*, *GE-21*, 94-101, 1983.

Welch, R. M., S. K. Sengupta, and D. W. Chen, Cloud field classification based upon high spatial resolution textural features, 1, Gray level co-occurrence matrix approach, *J. Geophys. Res.*, *93*(D10), 12,663-12,681, 1988.

Welch, R. M., M. S. Navar, and S. K. Sengupta, The effect of spatial resolution upon texture-based cloud field classifications, *J. Geophys. Res.*, *94*(D12), 14,767–17,781, 1989.

Weszka, J. S., C. R. Dyer, and A. Rosenfield, A comparative study of texture measures for terrain classification, *IEEE Trans. Sys. Man. Cybern.*, *SMC-6*, 269-285, 1976.

Wu, R., J. A. Weinman, and R. T. Chin, Determination of rainfall rates from GOES satellite images by a pattern recognition technique. *J. Atmos. Oceanic Tech.*, *2*, 314-330, 1985.

J. Key, Cooperative Institute for Research in Environmental Sciences, University of Colorado, Boulder, Colorado 80309-0449.

(Received March 1, 1989;
revised November 7, 1989;
accepted November 9, 1989.)